View metadata, citation and similar papers at core.ac.uk
brought to you by CORE
provided by CiteSeerX

JOURNAL OF GEOPHYSICAL RESEARCH, VOL. 109, E05002, doi:10.1029/2004JE002242, 2004

Crater degradation in the Martian highlands: Morphometric analysis of the Sinus Sabaeus region and simulation modeling suggest fluvial processes

Nancy K. Forsberg-Taylor[1] and Alan D. Howard
Department of Environmental Sciences, University of Virginia, Charlottesville, Virginia, USA

Robert A. Craddock
Center for Earth and Planetary Sciences, National Air and Space Museum, Smithsonian Institution, Washington, D. C., USA

Received 26 January 2004; revised 17 March 2004; accepted 5 April 2004; published 12 May 2004.

[1] Results from simulation modeling of crater degradation by fluvial and eolian processes are compared with size-frequency and depth of infilling statistics for the heavily cratered Sinus Sabaeus quadrangle of Mars. The fractional degree of infilling of craters greater than 10 km in diameter in this region is bimodal, with a small population of post-Noachian craters with little infilling, whereas most Noachian craters are strongly infilled. This pattern is most consistent with fluvial erosion of craters, because modeling indicates that craters fill rapidly at first, but the rate of infilling diminishes through time as crater wall heights diminish and the area of deposition on the crater floor increases. Simulated rates of crater infilling by eolian processes are more constant, which would be expected to produce craters equally distributed in degree of infilling, which is not observed. The small slope of the size-frequency distribution in the 10–30 km size range is also consistent with the more rapid fluvial erosion of smaller craters. The analysis also suggests that rates of crater production and of crater degradation were in rough balance during the Noachian epoch in the 10–30 km size range. *INDEX TERMS:* 5415 Planetology: Solid Surface Planets: Erosion and weathering; 5420 Planetology: Solid Surface Planets: Impact phenomena (includes cratering); 6225 Planetology: Solar System Objects: Mars; 1824 Hydrology: Geomorphology (1625); 1815 Hydrology: Erosion and sedimentation; *KEYWORDS:* craters, degradation

Citation: Forsberg-Taylor, N. K., A. D. Howard, and R. A. Craddock (2004), Crater degradation in the Martian highlands: Morphometric analysis of the Sinus Sabaeus region and simulation modeling suggest fluvial processes, *J. Geophys. Res.*, *109*, E05002, doi:10.1029/2004JE002242.

1. Introduction

[2] Since the first detailed pictures of the surface of Mars were returned by Mariner 4, the degraded nature of most Martian highland craters has been apparent. With the exception of relatively fresh post-Noachian craters, craters on the southern highlands generally demonstrate an absence of recognizable ejecta, low or missing crater rims, relatively flat crater floors, and much shallower depth than fresh craters of equivalent diameter. A variety of processes may have been involved in crater degradation, including superimposed impacts, weathering, mass wasting, fluvial incision and deposition, ice-related processes, lacustrine processes, lava infilling, eolian saltation, and airfall deposition from 1) dust storms, 2) ash from volcanic eruptions, or 3) regionally distributed ejecta from large impacts. Craters carry an important record of geomorphic processes acting on planetary surfaces because they are ubiquitous and, unless their rims are breached, their interiors represent a closed sedimentary system (an exception is eolian deflation of fine-grained sediments in a few impact craters [*Malin and Edgett*, 2000]).

[3] The processes and history of crater degradation in the Noachian is addressed in this paper by morphometric analysis of crater morphology in a portion of the cratered highlands coupled with simulation modeling of the two most widespread degradation processes, eolian (saltation and airfall) modification and fluvial erosion and deposition. We use as our study site the heavily cratered Sinus Sabaeus Quadrangle (0–30°S, 0–45°E) in which the dominant Noachian geomorphic processes were likely eolian modification (as broadly conceived to include both saltation and airfall) and fluvial erosion and deposition (including concomitant weathering and mass-wasting). At equatorial latitudes post-Noachian sedimentation and modification by ice-related processes [*Soderblom et al.*, 1973; *Mustard et al.*, 2001; *Head et al.*, 2003; *Kreslavsky and Head*, 2003] has apparently been negligible.

[4] Previous studies have argued for the predominance of fluvial erosion in the degradation of craters during the

[1]Now at Department of Earth and Planetary Sciences, Washington University, St. Louis, Missouri, USA.

Copyright 2004 by the American Geophysical Union.
0148-0227/04/2004JE002242$09.00

Noachian on the basis of channeling of the inner and outer crater rims, maintenance of a steep interior crater wall during degradation, inward-sloping crater floors with gradients typical of fluvial fans, and preferential destruction of the raised crater rim [*Craddock and Maxwell*, 1993; *Craddock et al.*, 1997; *Craddock and Howard*, 2002]. Further evidence for fluvial erosion is offered here on the basis of the frequency distribution of the amount of infilling of degraded craters and comparison with the results of simulation modeling.

[5] We first introduce the simulation models of eolian and fluvial crater degradation and investigate the temporal progression of relative crater degradation and the effect of initial crater size on the rate of infilling. We then present data on the frequency distribution of relative crater degradation in a representative area of the Martian highlands. On the basis of these data and comparison with the results of simulation modeling we conclude that the production of new craters and their erosional destruction by fluvial processes were roughly balanced during the Noachian, at least for craters smaller than 30 km in diameter.

2. Simulation Modeling of Crater Degradation

[6] A computer simulation program has been developed [*Howard*, 1994, 1997; *Craddock and Howard*, 2002] that simulates crater degradation by the processes of airfall deposition and by fluvial erosion and sedimentation. This simulation program is applied here to predict the temporal evolution of crater modification and the effects of crater size on modification rates. These predicted properties are then compared with measured properties of degraded craters in a portion of the Martian highlands.

2.1. Fresh Crater Morphology

[7] The initial conditions for the simulations are a single crater of specified diameter superimposed on an otherwise flat surface. Craters are generated by a routine that simulates the gross geometric properties of Martian craters on the basis of published statistics on crater depth, rim height, and interior wall gradient [*Garvin et al.*, 2002, 2003]. The program uses power functions of elevation versus distance from the crater center or rim to simulate the crater shape. A certain level of random noise is superimposed on this geometric form, with the amount of noise going from zero at the crater center to a maximum at the rim, and declining beyond the rim. The program does not simulate central peaks, multiring basins, or wall terracing. Simulated craters ranged from 1 km to 100 km in diameter, with the corresponding cell size for the rectangular DEM ranging from 8 m to 800 m, so that the crater diameter was about half the dimensions of the 256 × 256 simulation domain. The top and bottom boundaries are periodic, as are the left and right boundaries. Figure 1a shows an example 50 km simulated crater, and Figure 2 shows example scaled profiles through craters of varying diameter.

2.2. Eolian Modification

[8] Airfall and eolian degradation are modeled by a heuristic set of rules that model deposition and erosion as a function of the degree of exposure of a given location. Locations on or near ridges or isolated peaks (e.g., crater rims) are either eroded by eolian stripping and abrasion or receive diminished rates of sedimentation compared to relatively sheltered locations, such as crater floors and lower walls, which undergo net aggradation. The degree of deposition or erosion at any location within or outside of a crater is a function of an "exposure index", I_e, which is based on a weighted sum of the gradients, S_i, between the local elevation, E, and that of surrounding locations, E_i:

$$S_i = [(E_i - E)/\Delta x_i], \tag{1}$$

where Δx_i is the distance to the nearby point. The exposure index, I_{ek}, for points lying along a transect, k, extending from the given location is given by

$$I_{ek} = \sum_{i=1}^{n} S_i e^{-\eta \Delta x_i} \Big/ \sum_{i=1}^{n} e^{-\eta \Delta x_i}, \tag{2}$$

where the parameter η governs the relative importance of nearby versus distant points in determining the exposure. In computing equation (2) for a given location, transects near the crater rim include locations both within and outside of the rim. Points that are not visible from the location (lying behind a closer high point) are not included. For computational efficiency exposure indices are calculated only along the eight cardinal and diagonal directions from a given point and the net exposure index, I_e, is the average of the eight I_{ek}. The rate of eolian erosion or deposition, $\partial z/\partial t|_e$ is a function of the exposure index (z is the vertical dimension). The functional dependence of the erosion rate utilized here is shown in Figure 3.

2.3. Fluvial Erosion and Deposition

[9] The modeling of fluvial erosion of impact craters is based on the model of *Howard* [1994, 1997] with components modeling physical or chemical weathering of rocks to form transportable colluvium, mass wasting by nonlinear creep, fluvial detachment, and fluvial transport and deposition. Parameters used for these simulations are based on terrestrial values in semi-arid or arid landscapes except for correcting for the difference in gravity between Mars and Earth.

[10] It is assumed that the materials below the surface (lava, sediments, ejecta, etc., collectively termed "bedrock") may be indurated, but can be weathered at a finite rate by physical or chemical processes to form colluvium. The rate of bedrock weathering, $\partial z_b/\partial t$, is assume to decrease exponentially with the thickness, H, of overlying colluvium:

$$\frac{\partial z_b}{\partial t} = K_b e^{-cH}, \tag{3}$$

where K_b is the intrinsic maximum weathering rate (a joint function of rock properties and climate), and c governs the rate of decay of weathering rate with colluvium thickness In accord with terrestrial observations [*Heimsath et al.*, 1997, 1999, 2000] in semi-arid landscapes c is set to 0.02 m^{-1}, while K_b is a variable parameter in the range of 0.02 to 0.0002 m/yr (Table 1). Conversion of bedrock to colluvium is assumed to be isovolumetric. Note that $\partial z_b/\partial t$ is the rate of lowering of the colluvial-bedrock contact, and when

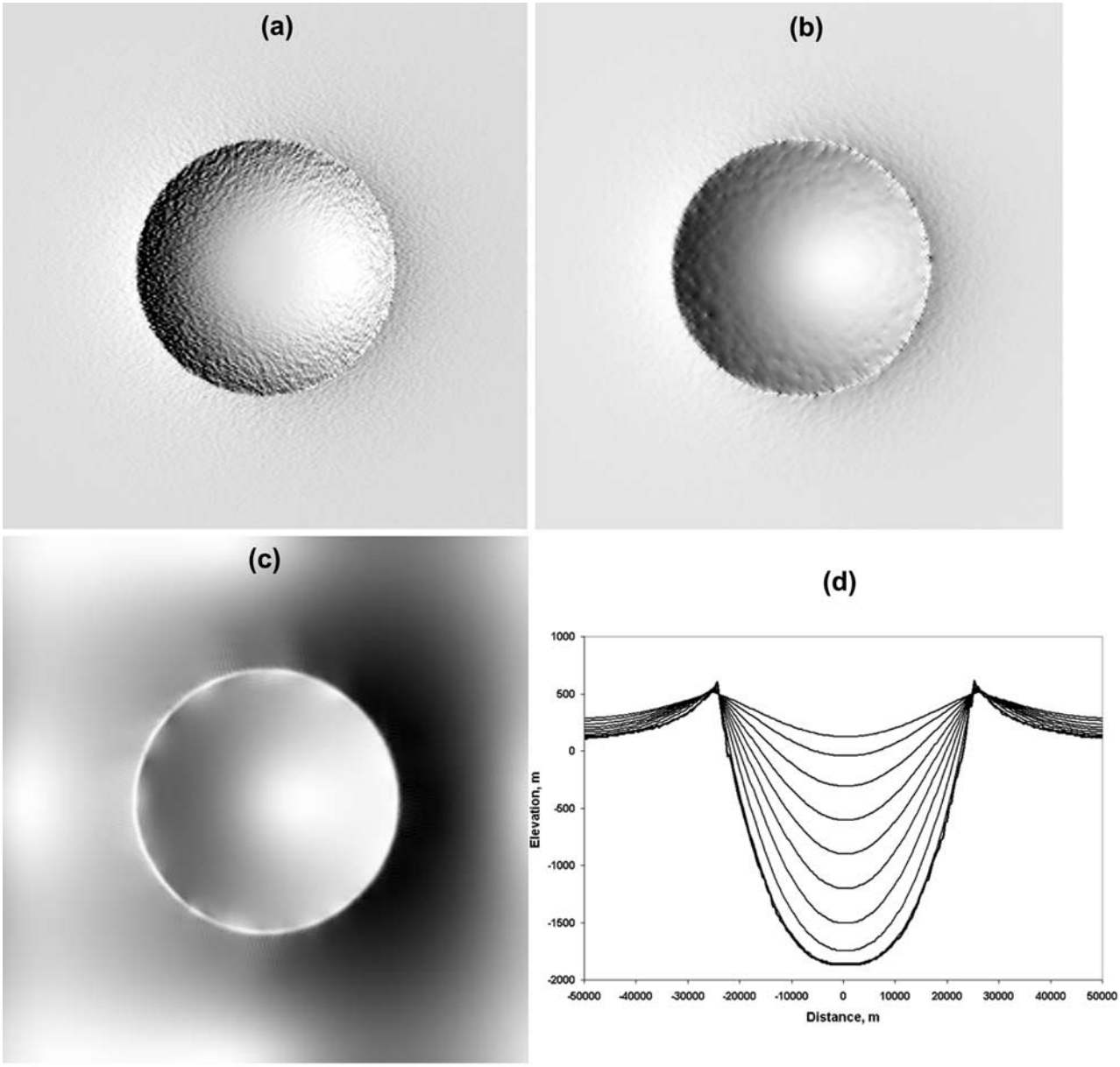

Figure 1. Simulated degradation of a 50 km impact crater (Figure 1a) through eolian infilling and erosion. Successive stages of infilling are shown in Figures 1b and 1c. Profiles through the center of the crater at equal time intervals are shown in Figure 1d.

weathering is isovolumetric it does not change the land surface elevation.

[11] Erosion by mass wasting, $\partial z_m/\partial t$, is proportional to the spatial divergence of colluvial mass flux, $\boldsymbol{q_m}$:

$$\frac{\partial z_m}{\partial t} = -\nabla \cdot \boldsymbol{q}_m. \tag{4}$$

Colluvial flux is given by a nonlinear relationship:

$$\boldsymbol{q}_m = \left[K_s|S| + K_f\left(\frac{1}{1-\{|S|/S_t\}^a} - 1\right)\right]\boldsymbol{s}. \tag{5}$$

where $|S|$ is the absolute value of local slope, $\boldsymbol{s}$ is the unit vector in the downslope direction, g is gravitational acceleration, S_t is a threshold gradient at which the rate of mass wasting becomes infinite (i.e., landsliding) (assumed to be 0.8), and K_s is creep diffusivity, which is assumed to be 0.0005 m^2/yr, characteristic of arid environments [e.g., *Carson and Kirkby*, 1972; *Martin*, 2000]. The influence of gravity on K_s is uncertain, but its influence should affect diffusivity by a maximum of a factor of 2.6. The exponent, a, is assumed to be 3.0, and K_f takes a value (0.5) that provides for a smooth but rapid approach to threshold slopes for rapid erosion rates. Erosion of bare bedrock slopes (exposed when erosion rates are greater than the maximum weathering rate given by equation (3)) follows equation (5), but with K_s set to zero and a critical gradient, S_t, of 2.7.

[12] Erosion by fluvial detachment, $\partial z_f/\partial t$ in bedrock channels and on steep slopes where the flow is carrying

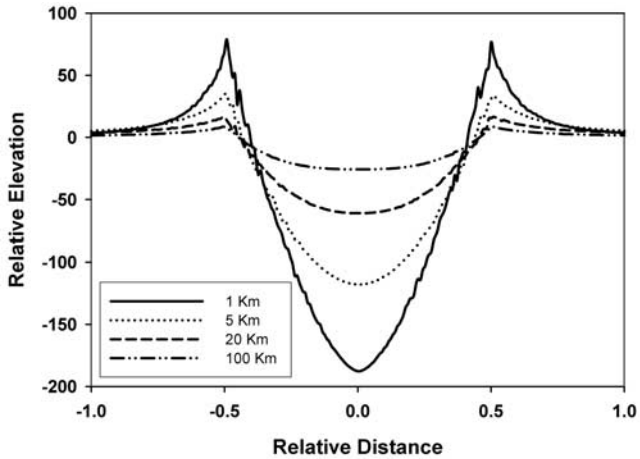

Figure 2. Profiles through simulated fresh impact craters of various diameters. The elevation and distance are geometrically scaled to the same relative distance.

less than a capacity load is assumed to be proportional to the shear stress, τ, exerted by flowing water, an assumption that is commonly used in simulation models and which has some empirical validation [*Howard and Kerby*, 1983; *Stock and Montgomery*, 1999; *Tucker and Whipple*, 2002; *van der Beek and Bishop*, 2003; *Tomkin et al.*, 2003]:

$$\frac{\partial z_f}{\partial t} = -K_f \tau, \tag{6}$$

where K_f is a variable parameter taking values from 0.02 to 0.0002 m^2 yr kg^{-1} (Table 1) when the reference shear stress is that which corresponds to the mean annual flood. This range encompasses measured terrestrial erosion rates in rocks ranging from shale to moderately strong sedimentary or metamorphic rocks (A. D. Howard, manuscript in preparation, 2004). Flow of water is assumed to be channelized and originating from runoff. Shear stress can be related to channel gradient and drainage area using

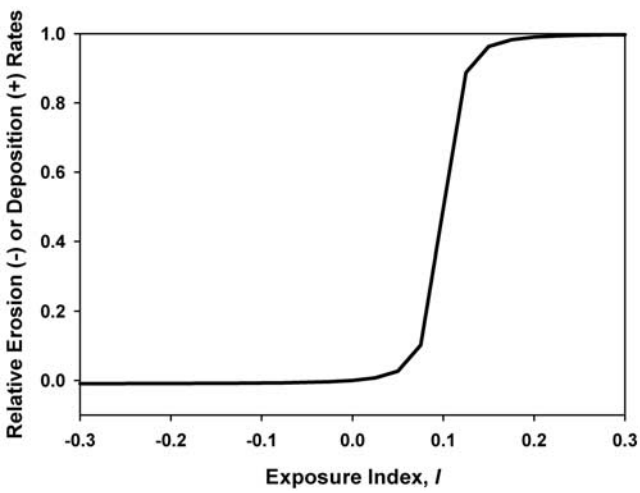

Figure 3. Modeled dependency of eolian deposition (positive) or erosion (negative) on exposure index, I_e.

Table 1. Values of Simulation Parameters

Run Type	K_b^a	K_f^b	K_r^c
Case 1	0.0002	0.02	1
Case 2	0.02	0.02	10
Case 3	0.02	0.02	1
Case 4	0.02	0.0002	10
Case 5	0.0002	0.0002	10

[a]Coefficient for rate of bedrock weathering in equation (3).
[b]Coefficient for rate of fluvial incision in equation (6).
[c]Ratio of colluvium erodibility to that of bedrock.

equations of hydraulic geometry and steady, uniform flow as discussed by *Howard* [1994]:

$$\tau = \rho_f g R S, \tag{7}$$

$$V = K_n g^{1/2} R^{2/3} S^{1/2} / N, \tag{8}$$

$$Q = RWV, \tag{9}$$

$$Q = PA^e, \tag{10}$$

$$W = K_w Q^b, \tag{11}$$

where R is hydraulic radius, S is channel gradient, V is mean velocity, N is Manning's resistance coefficient, P is a specific runoff yield (depth per unit area per unit time), Q is an effective discharge, W is channel width, A is drainage area, and K_n, K_p, K_a, K_w are coefficients. These coefficients and exponents are assumed temporally and spatially invariant. The following parameter values are assumed: $N = 0.03$, $K_n = 0.3$ (for metric units); $P = 3.0 \times 10^{-5}$ $m^{1.6}$/s, $e = 0.7$, $b = 0.5$, and $K_w = 5.0$ $s^{0.5}$ $m^{-0.5}$. Weathered bedrock (colluvium) is assumed to be a factor K_r more erodible than bedrock. The erodibility factor, K_r, is a parameter of the model with assumed values of 1.0 (equal erodibility) and 10.0 (Table 1).

[13] When the flux of sediment transported as bed and suspended load reaches or exceeds the transporting capacity of the flow (an alluvial channel as opposed to a bedrock channel), the erosion or deposition rate, $\partial z_a/\partial t$, is proportional to the spatial divergence of transport flux $\boldsymbol{q_s}$ (volume per unit time per unit width):

$$\frac{\partial z_a}{\partial t} = -\nabla \cdot \boldsymbol{q}_s. \tag{12}$$

[14] Sediment transport flux is estimated using a bedload transport formula that expressed as the relationship between a dimensionless transport rate, Φ, and a dimensionless shear stress, τ^* [e.g., *Yalin*, 1977]:

$$\Phi = K_e \{\tau^* - \tau_c^*\}^p, \tag{13}$$

where

$$\Phi = \frac{q_{sb}(1-\mu)}{g^{1/2} d^{3/2} (S_s - 1)^{1/2}} \text{ and } \tau^* = \frac{\tau}{\rho_f g (S_s - 1) d}. \tag{14}$$

In these equations τ_c^* is the value of τ^* at the threshold of motion, q_{sb} is bed sediment transport rate in bulk volume of sediment per unit time per unit channel width, S_s is the specific gravity of the sediment, g is gravitational accelera-

tion, ρ_f is the fluid density, d is the sediment grain size, and μ is alluvium porosity. A dominant bed grain size of 0.02 m is assumed, with $K_e = 8.0$, $p = 1.5$, $\tau_c^* = 0.05$, and $S_s = 2.65$. The shear stress is estimated from equations (7)–(11), with the dominant discharge for sediment transport assumed to be 0.6 of the mean annual flood, flowing 2% of the year. The bed sediment load is assumed to constitute 20% of sediment eroded from slopes.

[15] In bedrock channels the overall erosion rate, $\partial z/\partial t$, is a weighted function of the rates of mass wasting and fluvial erosion, as discussed by *Howard* [1994, 1997]. Where channel gradients are low enough that channels transport a capacity bedload, erosion and deposition rates are governed by equation (12). For the simulations reported here, the climate was assumed to be sufficiently arid that no standing water was present for appreciable periods of time within the crater, and that runoff characteristics are typical of terrestrial deserts or periglacial environments.

[16] Making different assumptions about the values of most of the simulation parameters will affect absolute erosion rates and details of crater morphology, but will have little effect on the issues most relevant to this study, that is, relative infilling rates of craters of different sizes and the temporal changes in infilling rates through time. The model parameters that most affect these properties are the relative rates of rock weathering (K_b), rock fluvial erodibility (K_f), and relative colluvium erodibility (K_r). A series of simulations were conducted for fluvial and mass wasting erosion on craters of different sizes with several combinations of these parameters (Table 1). For more information on model details and scaling, see *Howard* [1994].

2.4. Simulation Results

[17] Although attempts have been made to characterize absolute rates of Martian crater modification by eolian and fluvial processes [*Barlow*, 1995; *Golombek and Bridges*, 2000], the simulation results reported here are presented in relative terms, either as amounts of modification through time assuming constancy of process rates or the relative rates of degradation for craters of different size. Both eolian and fluvial processes may have been highly variable both in time and location due to effects of gradual climate deterioration during the Noachian, quasiperiodic climate change and, possibly, the effects of short-term increase of global temperatures and precipitation rates by large impactors [*Segura et al.*, 2002].

2.4.1. Eolian Degradation

[18] The eolian model presented above is assumed to represent in a general way the long-term effects of crater modification by eolian processes, including airfall deposition of eolian dust, volcanic ash, or impact-produced debris transported over long distances. In addition, the long-term progression of crater filling by saltating sand is also assumed to be approximated by the model. However, the model does not attempt to represent the physics of eolian transport and deposition that modify craters, nor is the model mass-conserving. Nonetheless, the resulting pattern of crater infilling resembles images of many modified Martian craters. Figure 1 shows a crater with simulated eolian infilling, Figure 4 shows small Martian craters with obvious eolian deposition, and

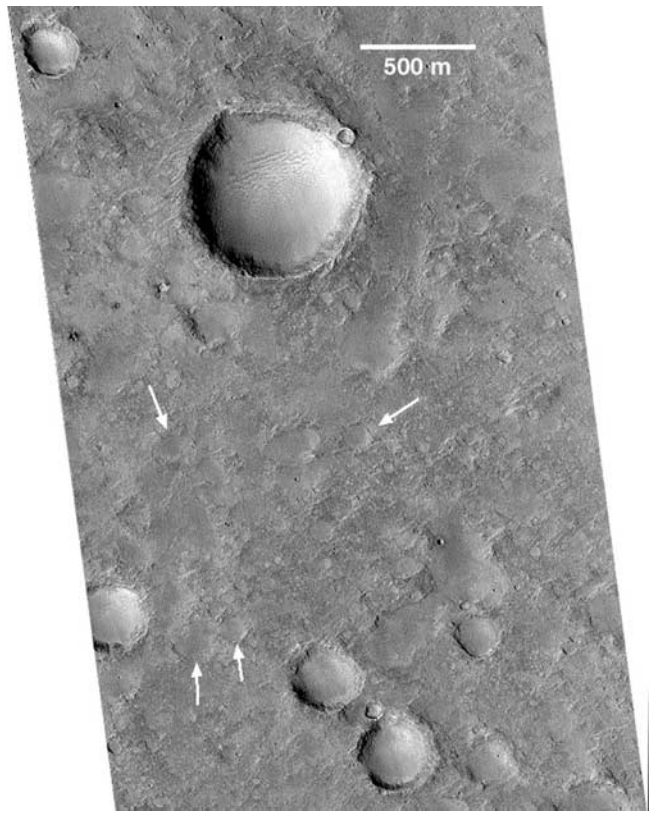

Figure 4. Small impact craters in the Isidis region filled with eolian deposits. MOC NA image M0404177, located at about 1.4°N, 91°E. Small craters (arrows) are nearly infilled, while larger craters are only partially filled. Parallel ridges visible in the largest crater are eolian dunes or megaripples.

Figure 1d shows successive profiles of eolian blanketing during one simulation. A general characteristic of the simple eolian infilling is that the crater rims remain largely clear of deposits, whereas the crater center becomes filled with a deposit having a generally parabolic cross-section. Obviously the crater diameter remains unchanged during eolian modification. In the simulations reported here eolian crater rim erosion is assumed to be small (Figure 3).

2.4.2. Fluvial Degradation

[19] Simulated fluvial modification infills the crater bottom with alluvial fan deposits, whereas the crater rim gradually backwastes while maintaining a generally steep slope. Depending on the model parameters, the interior crater wall may be strongly gullied (Figure 5) or relatively smooth (Figure 6). Similar variations occur in Martian degraded craters (compare Figure 5 with Figure 7 and Figure 6 with Figure 8). Both the backwasting and the downcutting of the crater rim occur, so that in later stages of erosion the crater may become essentially rimless. Example craters degraded by fluvial erosion are shown in Figures 5 and 6. Successive profiles are shown in Figures 5d and 6d. Many strongly degraded Martian highland craters in the size range of 10–150 km exhibit both relatively steep inner walls, an inward-sloping crater floor, and fluvial gullying on the crater walls (e.g., Figure 7), suggesting fluvial erosion

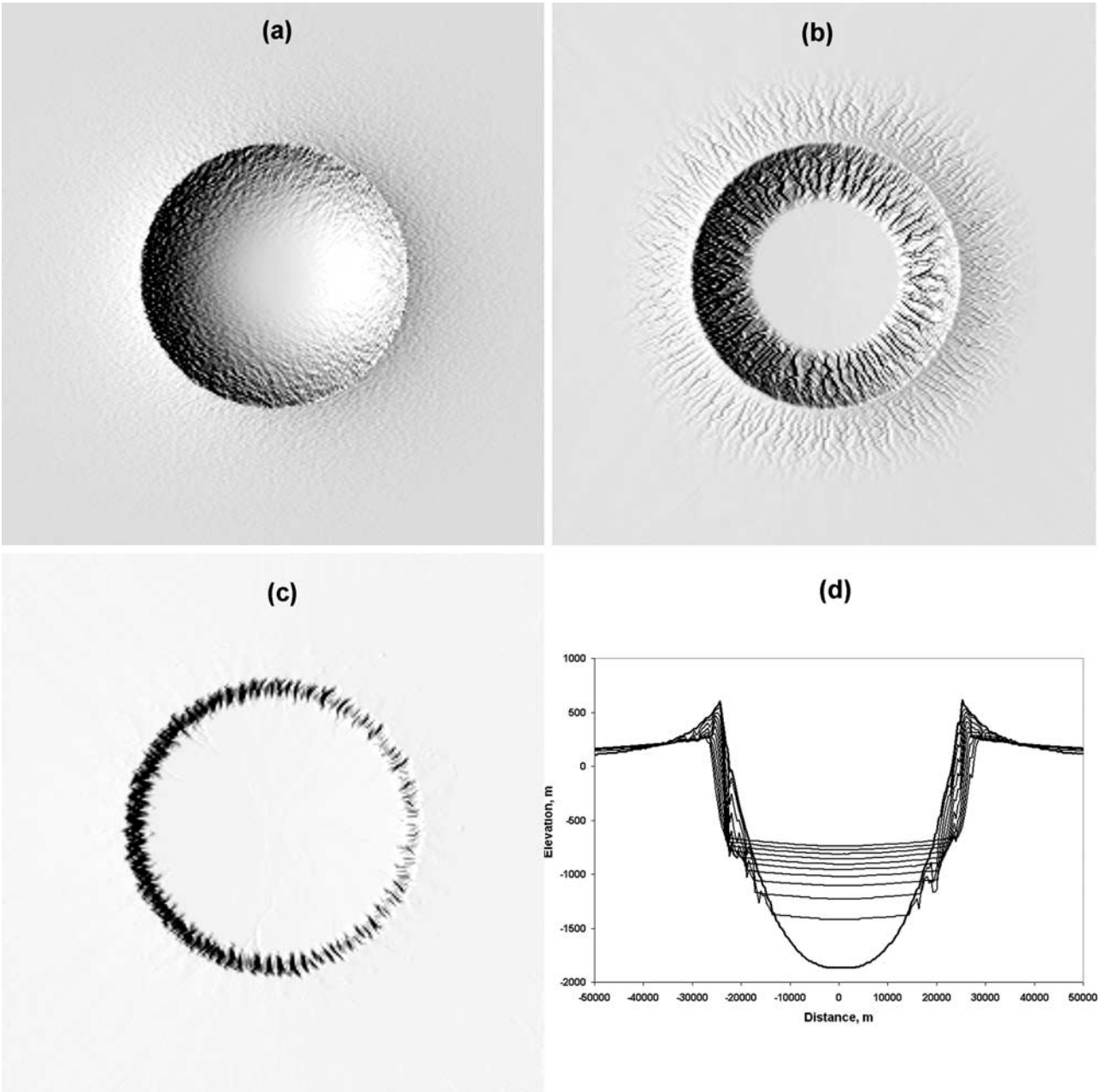

Figure 5. Simulation of degradation of a 50 km impact crater (Figure 1a) by fluvial erosion, mass wasting, and fluvial sediment deposition. Successive stages of erosion are shown in Figures 5b and 5c. Crater diameter has increased by about 20% by the stage shown in Figure 5c. Figure 1d shows profiles through the center of the crater at equal temporal intervals. Colluvium and bedrock are assumed to have equal erodibility.

has been the dominant modifying process [*Craddock and Maxwell*, 1993; *Craddock et al.*, 1997; *Craddock and Howard*, 2002].

2.4.3. Crater Infilling Rates and Their Diameter Dependency

[20] A series of simulations were conducted with both the fluvial and eolian degradation models to determine the temporal progression of crater modification and the dependency of initial crater diameter on infilling rates. In these simulations the intrinsic rate constants for the modification were assumed to be temporally constant and to be the same for initial craters of different size. The relative degree of crater modification was expressed as the ratio R,

$$R = \frac{(H - h)}{H}, \tag{15}$$

where H is the initial fresh crater depth (measured from the average rim height to the lowest point of the crater floor) and h is the crater depth at any subsequent time. For a fresh crater this ratio is zero, and for a completely degraded crater the ratio approaches unity. Note that a

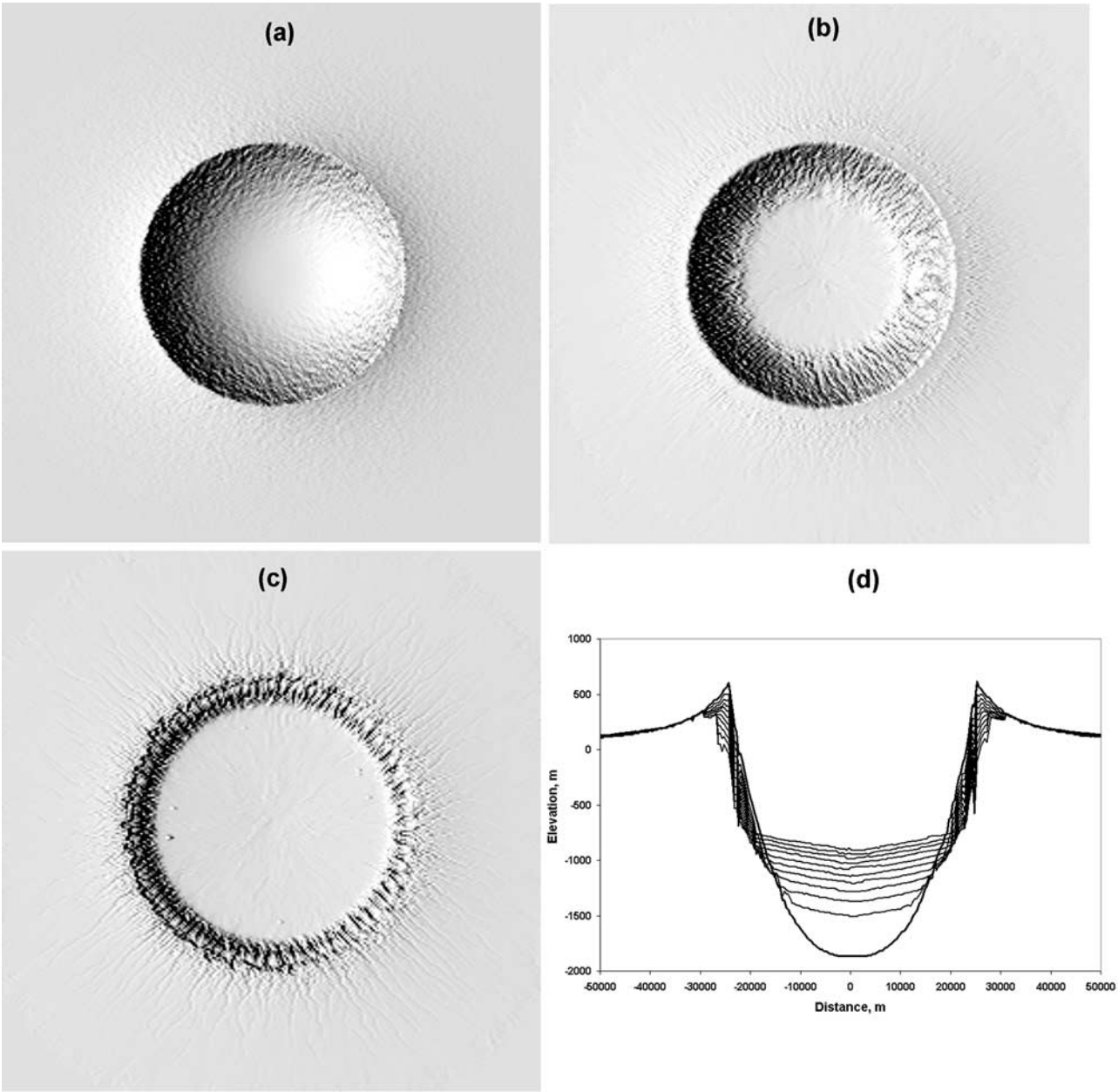

Figure 6. Simulation of degradation of a 50 km impact crater (Figure 6a) by fluvial erosion, mass wasting, and fluvial sediment deposition. Explanation similar to Figure 5 except that colluvium produced by weathering is assumed to be 10 times more erodible than bedrock, and bedrock becomes exposed in the walls and rim of the crater.

reduction in crater depth can occur both by infilling and by rim erosion, although the magnitude of the former dominates for simulations of both fluvial and eolian degradation.

[21] For small craters the simulated eolian crater infilling was nearly linear with time, but for large craters the rate of infilling was slower near the beginning and end of the simulation, presumably due to the shallower relative depth (Figure 9). Simulations were conducted with model craters of 1, 2, 5, 10, 20, 50, and 100-km diameters whose initial geometry was given by the *Garvin et al.* [2003] fresh crater scaling. The results were used to create multiple regression models, utilized to predict the actual simulation time, T, at various values of relative crater depth, R, and the corresponding crater diameter, D. The resulting equation for eolian infilling is

$$T \propto D^{0.66} R^{0.77}, \tag{16}$$

which explains 99% of the variation in simulation time (r^2 = 0.99). The multiplicative constant is not reported because the absolute modification rates for Martian craters are uncertain and presumably varied with location and certainly through geologic time. Because of the initially slow infilling rate, which might be model dependent, an additional model was fit to the later stages of eolian infilling in which

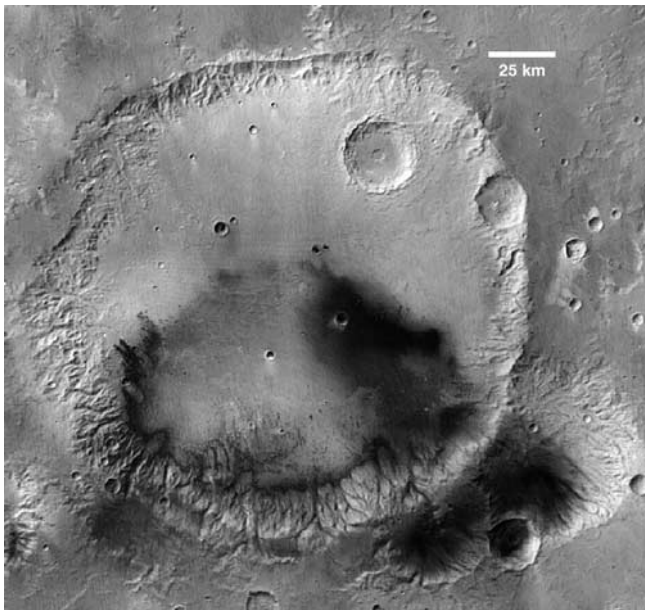

Figure 7. A portion of the MOC WA MOC wide-angle image of a 190 km, fluvially dissected crater (Dawes) in the Sinus Sabaeus region at 8°S and 39°E.

infilling was assumed to be linear with time. The resulting model is

$$\frac{(T - T_{0.1})}{(R - R_{0.1})} \propto D^{0.41}, \left(r^2 = 0.96\right) \tag{17}$$

where $T_{0.1}$ is the simulation time at which the relative crater modification R equals 0.1 ($R_{0.1}$). These results indicate a less than linear dependence of relative infilling on initial crater diameter. Initial models of crater infilling by eolian

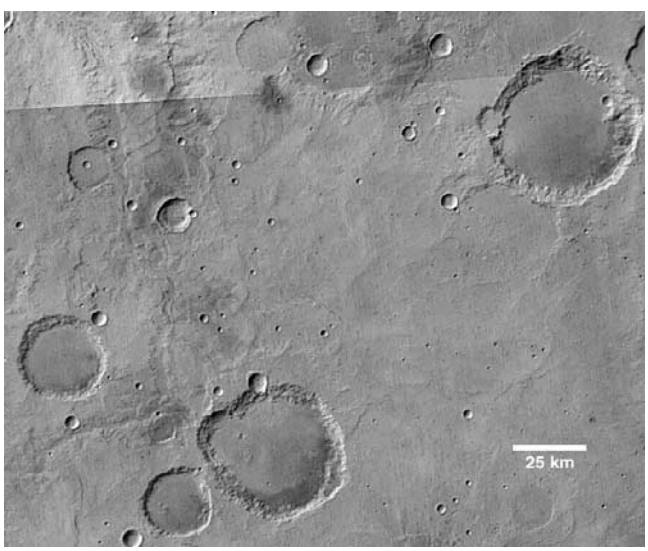

Figure 8. A portion of the MOC WA image mosaic of the Sinus Sabaeus quadrangle centered at 18°S and 6°E, showing degraded craters with steep interior rims and possible rock outcrops with only modest gully development.

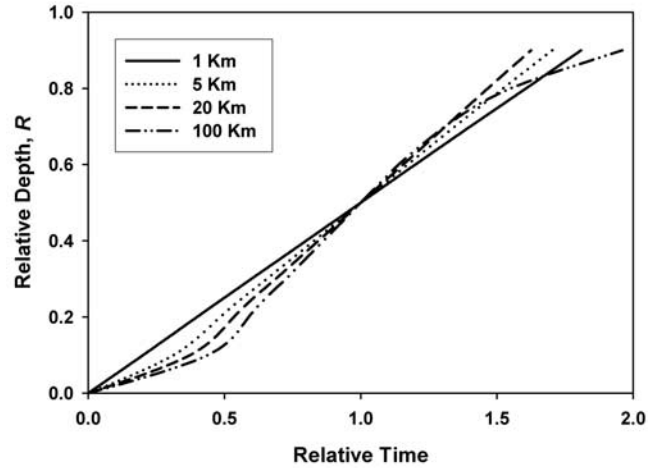

Figure 9. The degree of relative infilling, R, of the crater (defined in equation (15)) as a function of relative time during simulations of eolian degradation, with time during runs with different initial size scaled so that $R = 0.5$ at unity relative time.

deposition [*Hartmann*, 1971; *Opik*, 1965, 1966] assumed a linear dependency of infilling time with crater diameter under the presumption that crater depth scaled linearly with diameter. *Hartmann* [1999] and *Hartmann et al.* [1999] later revised the predicted infilling times to reflect the less than linear increase of crater depth with diameter. The global fresh crater statistics collected from MOLA observations [*Garvin et al.*, 2003] suggest $H \propto D^{0.8}$ for simple craters less than 7 km in diameter and $H \propto D^{0.5}$ for larger, complex craters. Thus equation (16) is reasonably consistent with the assumption that the eolian deposition rate in craters is independent of crater size.

[22] For crater modification by fluvial erosion and deposition interpretation of relative infilling, R, is complicated by the increase of the crater diameter through time due to rapid erosion of the steep inner crater wall. For Martian degraded craters only the present diameter is known. Therefore using the present degraded crater diameter to predict the initial fresh crater depth will yield somewhat greater depths than the actual initial value if the degradation occurred by fluvial erosion. In the simulations of fluvial crater degradation the crater diameter enlarged by about 5% when R was in the range 0.4 to 0.5, but then increased rapidly to about 20% by $R \sim 0.7$ (e.g., Figure 5). Therefore two sets of regressions were run for temporal variation of crater infilling by fluvial processes, the first using (15) with H being the actual initial crater depth, and another regression for R',

$$R' = \frac{(H' - h)}{H'}, \tag{18}$$

where H' is the fresh crater depth predicted using the observed crater diameter at the given time during the simulation. The resulting regressions using R' proved to be statistically indistinguishable from those using R, so we report only results using R.

[23] Several sets of process-related parameters were used with the simulation model, varying the parameters K_f, K_b,

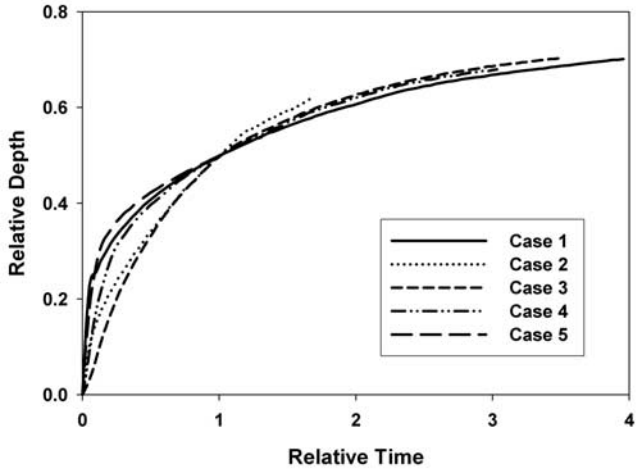

Figure 10. The temporal progression of crater infilling for simulated fluvial erosion of a 50 km impact crater. Times for various sets of process and material parameters (see Table 1) are scaled so that relative depth is 0.5 at a relative time of unity.

and K_r (Table 1). The temporal progression of R is shown for several simulations of erosion of a 50 km crater (Figure 10). Although there is considerable variability in the shape of the curves, they all differ from the eolian modification in that the infilling rate diminishes with time. This occurs primarily because the source region for the sediment filling the crater (the inner crater wall) diminishes in height during the simulation, and secondarily because erosion increases the crater diameter so that the area over which sediment is deposited increases. A set of simulations for various initial crater diameters were conducted for two sets of parameters (Cases 1 and 2 in Table 1). Regressions for the simulated time at given values of progressive infill yielded the following equations:

$$\text{Case 1}: \quad T \propto D^{1.96}R^{2.52}, \left(r^2 = 0.94\right) \tag{19}$$

$$\text{Case 2}: \quad T \propto D^{1.17}R^{1.44}. \left(r^2 = 0.98\right) \tag{20}$$

Although considerable variation in the exponents occurs for different sets of simulation parameters, the two cases presented are representative of two endpoints. For Case 1 the colluvium is as easily eroded as bedrock or the weathering rate keeps pace with fluvial erosion, so that slopes are colluvium-covered, whereas for Case 2 the bedrock is 10 times less erodible than colluvium, and the rate of weathering is sufficiently slow that steeper crater walls expose bedrock. The Case 1 results are very similar to a simplified model in which the rate of sediment delivery to the crater floor is assumed to be proportional to the exposed area of the interior crater wall.

3. Crater Morphology and Crater Counts

[24] The Sinus Sabaeus Quadrangle (0°S to 30°S and 0°E to 45°E) was selected as a representative highly cratered region to characterize the morphometry of all recognizable fresh and degraded craters greater than 10 km in diameter. Craters were identified and classified from Viking-based MDIM 5° × 5° quadrangle images supplemented by topographic contour maps of the same quadrangles made from MOLA observations. In this quadrangle 530 craters were analyzed for a range of morphometric parameters. Individual MOLA tracks were utilized rather than gridded data to avoid artifacts due to sparse data. An additional 320 craters were included in crater counts but were not morphometrically analyzed because of 1) poor MOLA coverage; 2) strong modification by later impacts, or 3) breaching of the crater wall by entering or exiting fluvial channels (not a closed depositional system). Each crater was visually assigned a degree of degradation using the standard classification system [*Craddock and Maxwell*, 1993; *Craddock et al.*, 1997; *Barlow et al.*, 2000], ranging from "A" for fresh to "E" for highly degraded craters. Qualitative characteristics were used in conjunction with the quantitative morphometric measurements to examine the properties of crater modification within the quadrangle as a function of crater diameter, location within the quadrangle and elevation. A variety of measurements and analyses were conducted [*Forsberg*, 2003], but we report here results related to determining the processes responsible for degradation.

3.1. Observed Frequency of Relative Infilling

[25] The frequency distribution of the estimated degree of crater infilling, R, for craters in the 10–100 km diameter range within the Sinus Sabaeus Quadrangle is noteworthy in its bimodal character, with a peak near R = 0.05 (relatively fresh craters) and another, higher peak near R = 0.6 to R = 0.8 (Figure 11). The first peak (R = 0.5) is largely composed

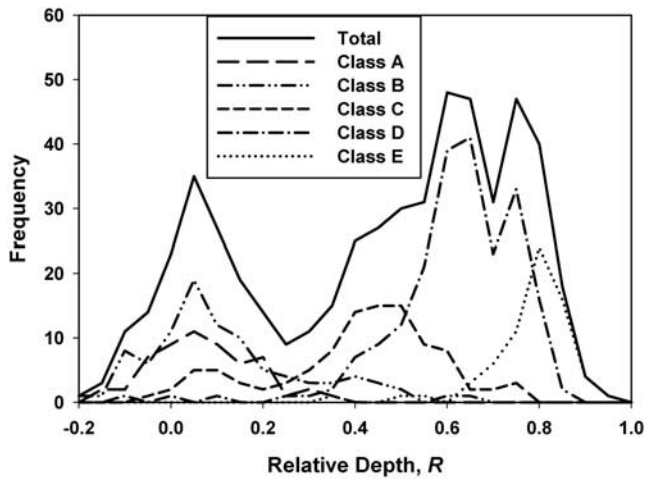

Figure 11. Frequency distribution of relative depth, R, for fresh and degraded impact craters in the Sinus Sabaeus Quadrangle. The original fresh crater depth, H, for each crater is estimated from relationships derived from MOLA topography [*Garvin et al.*, 2003]. Note that negative values of R can occur because H is estimated from global relationships that do account for regional or target material influences on the original depth of individual craters. Separate curves are shown for craters falling in the classes A (fresh) to E (highly degraded) as well as the total crater population. Degradation classification is based on visual crater characteristics in images with 200–400 m/pixel resolution.

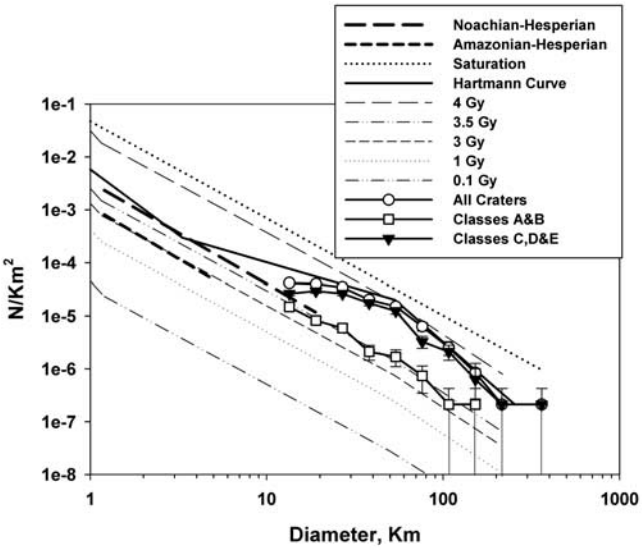

Figure 12. Size-frequency diagram for impact craters in the Sinus Sabaeus Quadrangle. This plot uses the Hartmann technique of counting all craters in size intervals proportional to the square root of crater diameter. Separate curves are shown for all craters greater than about 10 km in diameter, and separate curves are shown for impact craters classified in degradation classes A and B as well as all craters in classes C through E. For reference the plot shows the crater production curves estimated by *Hartmann* [1999] and *Hartmann and Neukum* [2001], the estimated saturation curve, the boundaries between the Noachian and Hesperian and the Hesperian and Amazonian [*Tanaka*, 1986; *Tanaka et al.*, 1988], and an empirical curve for crater density on the Martian highlands from *Hartmann* [1999] and *Hartmann et al.* [1999].

of craters visually classified as fresh or very slightly degraded (Classes A and B), whereas the higher peak is composed of visually moderately to highly degraded craters (Classes C, D, and E). The strong correspondence between the letter classification system based on visual characteristics of craters and the quantitative measurement of crater depth from MOLA topography indicates that the visual classification is a reliable indicator of degradation state. The lack of appreciable degradation and the size frequency distribution of craters in Classes A and B (Figure 12) are consistent with their constituting the population of post-Noachian craters within the region. The distribution of the remaining craters, presumably the Noachian population, thus displays strong negative skewing, indicating most of the craters are highly degraded. Also noteworthy is that the shape of this bimodal distribution does not appear to be a strong function of crater diameter within the range of 10–30 km diameter craters (Figure 13).

[26] A variety of Noachian temporal histories of crater production and degradation might have produced this distribution of crater degradation. Two end-members are explored here. The first is that this distribution resulted from degradation of a production (or, possibly saturation) population of fresh impact craters by a short-lived episode of modification late in the Noachian. This *episodic* model seems inconsistent with the lack of difference in the shape of the degradation frequency function, R, with crater diameter. Equations (19) and (20) above indicate that both eolian and fluvial modification act more swiftly on smaller craters. If the episodic model were appropriate, then the distribution of R values for smaller craters should be more negatively skewed than for larger craters.

[27] The other model to be explored is the *steady state* model, in which the rate of crater production and degradation were proportional to each other (although not necessarily temporally constant). Assuming that elapsed time, T, to a given degradation state, R, is a power function with exponent β (e.g., equations (16), (17), (19), and (20)), the frequency of craters in a given degradation state, $f(R)$, should be proportional to $\partial T/\partial R$,

$$f(R) \propto \frac{\partial T}{\partial R} \propto R^{\beta-1}. \tag{21}$$

Thus, for example, a simple model of a constant rate of crater floor buildup, such as was proposed by *Opik* [1965, 1966] and *Hartmann* [1971] as representing eolian deposition ($\beta = 1$) would give a uniform frequency distribution of observed craters as a function of R (Figure 14). The simulation modeling of eolian crater infilling (16) suggests $\beta = 0.77$, giving a slightly positively skewed distribution (Figure 14). Fluvial infilling modeling, on the other hand, suggests $\beta \geq 1.4$ (19 and 20), producing a negatively skewed distribution. The frequency distribution for Case 1 fluvial simulations is more similar to the observed distribution of R for degradation classes C through E in the range $0 < R < 0.8$ than are the Case 2 simulations (compare Figures 11 and 14). The less strongly skewed distribution for Case 2 simulations occurs because erosion rates are limited by the rapidity of bedrock weathering. We conclude that, if the steady state model is reasonably accurate, fluvial degradation was primarily responsible for degradation of Noachian craters in the 10–100 km diameter range, and that the rate of crater degradation was not strongly limited by the rate of

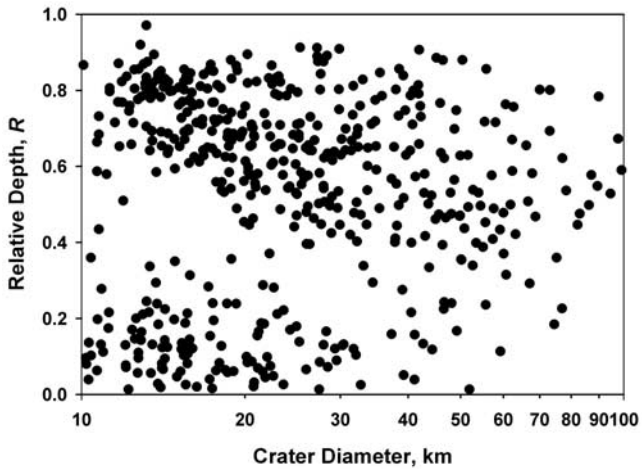

Figure 13. Distribution of relative depth with crater diameter, showing the strongly bimodal distribution for craters with diameters less than 30 km. The number of fresh craters greater than 30 km diameter is insufficient to assess the bimodality.

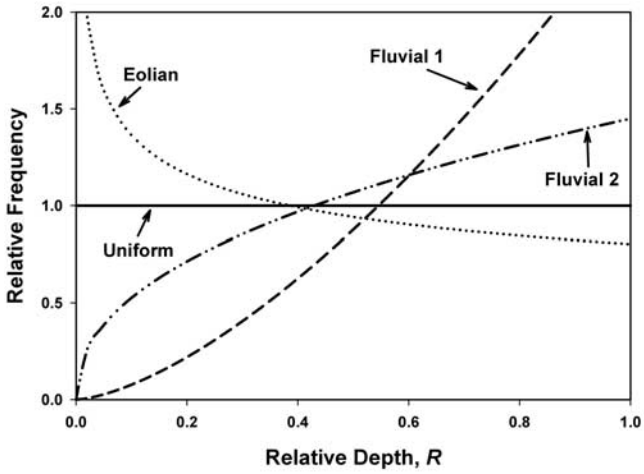

Figure 14. Models of the expected frequency of craters of various degrees of degradation (measured by relative depth, R) for various degradation processes. Curves assume a steady state balance between crater production and crater degradation. Uniform rate corresponds to degradation following equation (17), eolian for equation (16), Fluvial, Case 1 for equation (19), and Fluvial, Case 2 for equation (20).

conversion of bedrock to colluvium. Clearly, however, eolian infilling becomes dominant in degradation of small craters during the post-Noachian (e.g., Figure 4), and in some locations, such as Arabia, appreciable thickness of sedimentary deposits have been emplaced and eroded [*Moore*, 1990; *Malin and Edgett*, 2000]. The origin of these deposits is controversial but may be eolian.

[28] The downturn of the frequency distribution of Sinus Sabaeus craters for degradation state beyond $R = 0.8$ (Figure 11) can be attributed to several factors: 1) highly degraded craters are hard to recognize in images; 2) older craters are more likely to have been eradicated by later impacts or so strongly modified that crater shape statistics could not be collected; and 3) older craters are more likely to have their rim breached by fluvial drainage either entering or leaving the crater; we excluded such craters from our morphometric sample. The simulations are not subject to these exclusions, so that the frequency-relative depth curves (Figure 14) do not show a leveling and downturn for $R > 0.8$.

3.2. Size-Frequency Distribution of Craters

[29] The steady state model also has implications for the size-frequency distribution of craters in the Sinus Sabaeus area. If production and eradication of craters in a given size range are balanced, then the number of observed craters should be proportional to the average survival time, T, of craters of that size. If we estimate survival time by that duration required to reach an advanced state of degradation (say $R = 0.8$), then equations (16), (17), (19), and (20) can be used to predict the dependency of survival time on crater diameter. If the survival time is a power function of diameter with power μ,

$$T \propto D^{\mu}, \tag{22}$$

and the cumulative production rate $\partial N/\partial t$ (number $\geq$ D per unit area per unit time) is a power function of diameter with exponent ϑ, then the observed cumulative number density, N', should also be a power function equal to the product of production rate and survival time [*Hartmann*, 1971, 1999]:

$$N' \propto D^{\vartheta+\mu}. \tag{23}$$

Hartmann and Neukum [2001] suggest that $\vartheta = -1.8$ for crater production in the range $1 < D < 32$ km and $\vartheta = -2.2$ for $D > 32$ km. *Hartmann and Neukum* [2001] and *Hartmann et al.* [1999] have generated a synthetic size-frequency curve for ancient cratered terrain on Mars (Figure 12) under the assumption that eolian infilling dominates crater degradation in the range of 1 to 50 km, with a slope $N' \propto D^{-1.0}$, which is roughly consistent with our simulations of eolian sedimentation (17). Fluvial erosion should produce an even stronger reduction in the slope $\vartheta + \mu$ to values approaching zero (using exponents for μ from equations (19) and (20)). The size-frequency curve for the Sinus Sabaeus region is strongly convex in the region from 10 km to 70 km with the slope decreasing from zero in the 12–26 km range through -1.1 in the 26–50 km range to about -2.6 in the 50–100 km range (Figure 12). We interpret this distribution to imply a gradual transition from a production or saturation distribution for craters >50 km to a steady state fluvial degradation distribution in the 10–25 km range.

[30] As a cautionary note to the above analysis, some studies suggest that the downturn of crater frequency at small diameters on heavily cratered terrains may only be partially due to degradation. Differences in the size-frequency distribution of the impacting populations may be at least partially responsible for the downturn in crater density at diameters <50 km since some size-frequency distribution analyses of fresh impact craters on Noachian-aged units also display this downturn [see *Barlow*, 1990]). Our analysis of fresh class A and B craters in the Sinus Sabaeus Quadrangle, however, shows a linear trend in the size-frequency distribution in the >10 km size range that is consistent with *Hartmann*'s [1999] production function (Figure 12).

4. Conclusions

[31] Degradation of craters by fluvial erosion and deposition in simulations results in rapid initial infilling but a slowing rate through time (Figure 5) likely due to the decreasing height of interior crater walls and the increasing area of deposition as the crater enlarges due to crater wall erosion. By contrast, simulated eolian infilling occurs at a nearly constant rate (Figure 1). If the rate of crater production and crater degradation were roughly balanced during the Noachian, a dominance of degradation by eolian infilling would imply roughly equal numbers of craters (for a given size range) in all stages of infilling. However, if fluvial erosion were dominant, only a few craters would be in initial stages of infilling and most craters would be at advanced stages of sedimentation, with low crater walls. This pattern of large numbers of strongly degraded craters is, in fact, what is observed in the Sinus Sabaeus region of the Martian highlands (Figure 11).

[32] For both eolian and fluvial crater degradation the length of time required to produce any specified fraction of crater infilling increases with crater diameter. As a result, as

suggested by *Hartmann* [1971, 1999], the steepness of size-frequency crater curves should be reduced in those diameter ranges strongly affected by degradation. For the Sinus Sabaeus quadrangle the observed distribution of Noachian craters (Classes C, D, and E in Figure 12) is consistent with a gradual transition from a production or saturation distribution for craters >50 km to a steady state fluvial degradation distribution in the 10–25 km diameter range.

[33] In summary, our analysis of statistics of relative crater degradation and size-frequency distributions in the Sinus Sabaeus quadrangle confirms earlier conclusions that fluvial erosion was the dominant degradation process [*Craddock and Maxwell*, 1993; *Craddock et al.*, 1997; *Craddock and Howard*, 2002] and also suggests that rates of crater production and of crater degradation were in rough balance during the Noachian epoch. If future studies find that Noachian craters were significantly modified by other processes, such as ice induced glacier-like flow or energetic mass wasting, then our conclusions would need to be revised.

[34] **Acknowledgments.** This research was supported by the NASA Planetary Geology and Geophysics Program and the Mars Data Analysis Program.

References

Barlow, N. G. (1990), Constraints on early events in Martian history as derived from the cratering record, *J. Geophys. Res.*, *95*, 14,191–14,201.

Barlow, N. G. (1995), The degradation of impact craters in Maja Valles and Arabia, Mars, *J. Geophys. Res.*, *100*(E11), 23,307–23,316.

Barlow, N. G., J. B. Garvin, S. E. H. Sakimoto, R. O. Kuzmin, D. J. Roddy, L. A. Soderblom, J. M. Boyce, F. M. Costard, and R. A. Craddock (2000), Standardizing the nomenclature of Martian impact crater ejecta morphologies, *J. Geophys. Res.*, *105*(11), 26,733–26,738.

Carson, M. A., and M. J. Kirkby (1972), *Hillslope Form and Process*, 475 pp., Cambridge Univ. Press, New York.

Craddock, R. A., and A. D. Howard (2002), The case for rainfall on a warm, wet early Mars, *J. Geophys. Res.*, *107*(E11), 5111, doi:10.1029/2001JE001505.

Craddock, R. A., and T. A. Maxwell (1993), Geomorphic evolution of the Martian highlands through ancient fluvial processes, *J. Geophys. Res.*, *98*(E2), 3453–3468.

Craddock, R. A., T. A. Maxwell, and A. D. Howard (1997), Crater morphometry and modification in the Sinus Sabaeus and Margaritifer Sinus regions of Mars, *J. Geophys. Res.*, *102*, 13,321–13,340.

Forsberg, N. K. (2003), Analyses of crater morphologies and modification processes in the Sinus Sabaeus region of Mars, M. S. thesis, Univ. of Va., Charlottesville.

Garvin, J. B., S. E. H. Sakimoto, J. J. Frawley, and C. Schnetzler (2002), Global geometric properties of Martian impact craters, *Lunar Planet. Sci.*, *XXXIII*, abstract 1255.

Garvin, J. B., S. Sakimoto, and J. J. Frawley (2003), Craters on Mars: Global geometric properties from gridded MOLA topography, paper presented at Sixth International Conference on Mars, Calif. Inst. of Technol., Pasadena, Calif.

Golombek, M. P., and N. T. Bridges (2000), Erosion rates on Mars and implications for climate change: Constraints from the Pathfinder landing site, *J. Geophys. Res.*, *105*, 1841–1854.

Hartmann, W. K. (1971), Martian cratering III: Theory of crater obliteration, *Icarus*, *15*, 410–428.

Hartmann, W. K. (1999), Martian cratering VI: Crater count isochrons and evidence for recent volcanism from Mars Global Surveyor, *Meteorit. Planet. Sci.*, *34*(2), 167–177.

Hartmann, W. K., and G. Neukum (2001), Cratering chronology and the evolution of Mars, *Space Sci. Rev.*, *96*, 165–194.

Hartmann, W. K., L. Soderblom, P. Thomas, E. Danielson, P. James, J. Veverka, M. Malin, A. McEwen, and M. Carr (1999), Evidence for recent volcanism on Mars from crater counts, *Nature*, *397*(6720), 586–589.

Head, J. W., J. F. Mustard, M. A. Kreslavsky, R. E. Milliken, and D. R. Marchant (2003), Recent ice ages on Mars, *Nature*, *426*, 797–802, doi:10.1038/nature02114.

Heimsath, A. M., W. E. Dietrich, K. Nishiizumi, and R. C. Finkel (1997), The soil production function and landscape equilibrium, *Nature*, *388*(6640), 358–361.

Heimsath, A. M., W. E. Dietrich, K. Nishiizumi, and R. C. Finkel (1999), Cosmogenic nuclides, topography, and the spatial variation of soil depth, *Geomorphology*, *27*(1–2), 151–172.

Heimsath, A. M., J. Chappell, W. E. Dietrich, K. Nishiizumi, and R. C. Finkel (2000), Soil production on a retreating escarpment in southeastern Australia, *Geology*, *28*(9), 787–790.

Howard, A. D. (1994), A detachment-limited model of drainage-basin evolution, *Water Resour. Res.*, *30*(7), 2261–2285.

Howard, A. D. (1997), Badland morphology and evolution: Interpretation using a simulation model, *Earth Surf. Processes Landforms*, *22*(3), 211–227.

Howard, A. D., and G. Kerby (1983), Channel changes in badlands, *Geol. Soc. Am. Bull.*, *94*(6), 739–752.

Kreslavsky, M. A., and J. W. Head (2003), North-south topographic slope asymmetry on Mars: Evidence for insolation-related erosion at high obliquity, *Geophys. Res. Lett.*, *30*(15), 1815, doi:10.1029/2003GL017795.

Malin, M. C., and K. S. Edgett (2000), Sedimentary rocks of early Mars, *Science*, *290*, 1927–1937.

Martin, Y. (2000), Modelling hillslope evolution: Linear and nonlinear transport relations, *Geomorphology*, *34*(1–2), 1–21.

Moore, J. M. (1990), Nature of the mantling deposit in the heavily cratered terrain of northeastern Arabia, *Mars, J. Geophys. Res.*, *95*, 14,279–14,289.

Mustard, J. F., C. D. Cooper, and M. K. Rifkin (2001), Evidence for recent climate change on Mars from the identification of youthful near-surface ground ice, *Nature*, *412*, 4111–4114.

Opik, E. J. (1965), Mariner IV and craters on Mars, *Irish Astron. J.*, *7*, 92–104.

Opik, E. J. (1966), The Martian surface, *Science*, *153*, 255–265.

Segura, T. L., O. B. Toon, A. Colaprete, and K. Zahnle (2002), Environmental effects of large impacts on Mars, *Science*, *298*(5600), 1977–1980.

Soderblom, L. A., T. J. Kreidler, and H. Masursky (1973), Latitudinal distribution of a debris mantle on the Martian surface, *J. Geophys. Res.*, *78*(20), 4117–4122.

Stock, J. D., and D. R. Montgomery (1999), Geologic constraints on bedrock river incision using the stream power law, *J. Geophys. Res*, *104*(B3), 4983–4993.

Tanaka, K. L. (1986), The stratigraphy of Mars, *Proc. Lunar Planet. Sci. Conf. 17th*, Part 1, *J. Geophys. Res.*, *91*, suppl, E139–E158.

Tanaka, K. L., N. K. Isbell, D. H. Scott, R. Greeley, and J. E. Guest (1988), The resurfacing history of Mars: A synthesis of digitized, Viking-based geology, *Proc. Lunar Planet. Sci. Conf. 18th*, 665–678.

Tomkin, J. H., M. T. Brandon, F. J. Pazzaglia, J. R. Barbour, and S. D. Willett (2003), Quantitative testing of bedrock incision models for the Clearwater River, NW Washington State, *J. Geophys. Res.*, *108*(B6), 2308, doi:10.1029/2001JB000862.

Tucker, G. E., and K. X. Whipple (2002), Topographic outcomes predicted by stream erosion models: Sensitivity analysis and intermodel comparison, *J. Geophys. Res.*, *107*(B9), 2179, doi:10.1029/2001JB000162.

van der Beek, P., and P. Bishop (2003), Cenozoic river profile development in the Upper Lachlan catchment (SE Australia) as a test of quantitative fluvial incision models, *J. Geophys. Res.*, *108*(B6), 2309, doi:10.1029/2002JB002125.

Yalin, M. S. (1977), *Mechanics of Sediment Transport*, 298 pp., Pergamon, New York.

R. A. Craddock, Center for Earth and Planetary Sciences, National Air and Space Museum, Smithsonian Institution, Washington, DC 20560, USA. (craddock@nasm.si.edu)

N. K. Forsberg-Taylor, Department of Earth and Planetary Sciences, Washington University, St. Louis, MO 63130, USA. (nkforsbe@artsci.wustl.edu)

A. D. Howard, Department of Environmental Sciences, University of Virginia, P.O. Box 400123, Charlottesville, VA 22904-4123, USA. (ah6p@virginia.edu)